

Device-Specific Calibration Methods for Optical Frequency Domain Reflectometry-Based Shape Sensing in Catheters and Surgical Needles

Jacynthe Francoeur¹, Pierre Lorre², Iulian Iordachita¹, Raman Kashyap³ and Samuel Kadoury⁴

Abstract—Minimally invasive procedures for diagnosing and treating occlusive arterial diseases and prostate cancer face significant challenges due to the complexity of navigating within occluded arteries and precisely positioning surgical needles. Fiber optic sensors, coupled with optical frequency domain reflectometry (OFDR), offer promising solutions to the accuracy limitations of traditional imaging methods in complex anatomies. This work proposes custom calibration techniques of fiber optic sensors for vascular catheters and prostate surgical needles, addressing device-specific characteristics that can cause shape sensing inaccuracies, making precise and reliable calibration crucial. We assessed how calibration, tool characteristics, and spatial resolution affect shape reconstruction accuracy, with the catheter calibration protocol yielding a root-mean-squared-error (RMSE) of 1.67 ± 0.77 mm ($0.4\% \pm 0.2\%$), and the needle calibration protocol achieving 0.23 ± 0.14 mm ($0.2\% \pm 0.1\%$). Although the impact of spatial resolution wasn't significant, it's crucial to consider as it varies with the specific medical device and application.

Clinical relevance— The proposed calibration methods enhance the safety and precision of fiber optic minimally invasive procedures by reducing reliance on imaging like fluoroscopy, minimizing tool placement errors across various medical devices and clinical domains. We demonstrate potential for automation to improve both clinical outcomes and workflow efficiency.

I. INTRODUCTION

Minimally invasive procedures for diagnosing and treating occlusive arterial diseases and prostate cancer face technical challenges. Procedures like percutaneous transluminal angioplasty (PTA) use catheters to restore blood flow [1], but remain challenging for long occlusions due to catheter maneuvering and fluoroscopy limitations [2], [3]. Similarly, precise needle positioning in prostate cancer biopsies and therapies, typically guided by imaging techniques like transrectal ultrasound (TRUS) and MRI [4], is complicated by

needle-tissue interactions that can cause deviations, prolong procedures, and increase complications [5].

To address these procedural challenges, fiber optic sensors have gained popularity in recent years for the advantages they offer over conventional tracking methods, including the ability to detect a variety of physical parameters, small dimensions, immunity to electromagnetic interference and real-time capabilities [6]. Optical frequency domain reflectometry (OFDR), an interferometric technique that enables real-time and high-resolution strain measurement through the spectral analysis of the backscattered light in a fiber, holds promise for improving the accuracy and efficiency of minimally invasive procedures [7].

Previous studies explored fiber-optic shape sensing in surgical needle insertions [8]–[14] and flexible catheter monitoring [15]–[20], employing discrete and distributed measurement methods. Sensors may use multiple single-core fibers or pre-assembled multi-core fibers with 3 to 7 cores, embedded externally or internally within the devices.

Calibrating fiber optic sensors is essential for accurate and reliable feedback during procedures, as it corrects sensor variations, compensates for environmental factors, minimizes systematic errors, and establishes a consistent reference framework. In clinical tools, where millimeter-level errors matter, tailored calibration techniques are required to address their mechanical and functional differences. Catheters are long and flexible, designed to navigate complex anatomical pathways without causing tissue damage. They often rely on qualitative shape sensing to manage large, complex curvatures. In contrast, needles are short and rigid, optimized for precise tissue penetration and targeted navigation. They require quantitative shape sensing with strict adherence to boundary conditions to maintain accuracy, despite dealing with simpler shapes and smaller curvatures.

In the literature, fiber-optic calibration methods for shape sensing in minimally invasive surgical instruments face numerous challenges. A commonly used approach involves the Euler–Bernoulli approximation to relate wavelength shifts to strain across different planes. However, this method fails to adequately capture large deformations and variable curvatures encountered by surgical tools [9], [15]. Additionally, cross-sensitivity between strain and temperature necessitates compensation strategies, such as common-mode deduction [10], [12], temperature sensitivity characterization during calibration [20], or monitoring temperature variations in controlled environments [14], [19], which often struggle to generalize to clinical settings. Many calibration protocols also require specialized equipment, including tomography

*This work was supported by Boston Scientific Corporation, the Canadian Institutes of Health Research (CIHR) under grant No. MOP-451821, the Natural Sciences and Engineering Research Council (NSERC) and Fayolle Canada United-States' Prestige 2022-2023 Scholarship. This work was also supported by the National Institutes of Health under grant No. R01CA235134 and the Fonds de recherche du Québec – Nature et technologies.

¹Jacynthe Francoeur and Iulian Iordachita are with the Department of Mechanical Engineering, Johns Hopkins University, Baltimore, MD 21218, USA jfranc52@jh.edu, iordachita@jhu.edu

²Pierre Lorre is with the Department of Physics Engineering, Polytechnique Montréal, Montréal, QC H3T1J4, Canada pierre-2.lorre@polymtl.ca

³Raman Kashyap is with the Departments of Electrical Engineering and Physics Engineering, Polytechnique Montréal, Montréal, QC H3T1J4, Canada raman.kashyap@polymtl.ca

⁴Samuel Kadoury is with the Department of Computer and Software Engineering, Polytechnique Montréal, Montréal, QC H3T1J4, Canada samuel.kadoury@polymtl.ca

workbenches for precise fiber position determination [16], [21], or 3D templates, jigs, and phantoms [8], [9], [11], [12], [14], [19]. Procedures are often time-consuming, making integration into time-sensitive operating environments difficult. Moreover, boundary conditions, which are critical for ensuring accurate shape sensing, are frequently overlooked or insufficiently addressed. In summary, overcoming these challenges is crucial for improving the accuracy and reliability of fiber-optic shape sensing in clinical applications.

This work contributes to accurate fiber-optic shape sensing in robotic-assisted procedures by introducing a flexible calibration framework for both catheters and needles used in intravascular and prostate interventions. Using a custom fiber optic sensor with OFDR from [22], the work offers a comprehensive process to calibration, along with a detailed analysis of shape-sensing performance, analyzing factors such as spatial resolution, curvature and boundary conditions. The novelty of this work lies in the integration of one sensor prototype into two contrasting medical tools, enabling reliable shape sensing with clinically acceptable error margins. This study is the first to our knowledge to conduct a comparative analysis of calibration approaches for these two types of medical devices. It offers reproducible, device-specific solutions and provides a robust toolkit that will facilitate the adoption and optimization of fiber-optic shape sensing in minimally invasive medical procedures, while also establishing a foundation for refining calibration techniques in more complex environments or with other medical devices.

II. METHODS

A. Sensor fabrication

The optical fiber sensor was fabricated by first inscribing continuous chirped gratings with a random profile over 1.5 meters in three polyimide-coated optical fibers (155 μm OD, SM1250(10.4/125)P, Fibercore) using a femtosecond laser plane-by-plane writing technique [23]. This process enhanced the backscatter signal by about 40 dB, with a spectral response centered around 1540 nm. The fibers were embedded in a polymer (TOTAL M6823MZ) using a Leistritz twin-screw extruder [24], forming a robust and flexible 600 μm diameter sensor (Fig. 1a) with fairly stable fiber positions along its length [22].

For the catheter experiments, the sensor was inserted into a 1 m long 0.038" (0.97 mm) guidewire-compatible Terumo catheter and secured at both ends with shrink tubes to reduce mobility. For the surgical needle experiments, a sensor segment was initially inserted into a 635 μm ID nitinol tube. The minimal gap between the sensor and the tube effectively reduced movement and torsion risks, while optimizing strain transfer during deflection. Shrink tubing encased the proximal end to enhance structural integrity, and the stylet-needle connection was glued to the nitinol tube base. Strain signal noise was reduced by looping the proximal end of the fibers, which slightly reduced the signal amplitude and effectively eliminated unwanted ghost reflections. Additionally, to cancel noise-inducing reflections,

light-curing glue (AA 3922, Loctite, Henkel) was applied at the distal end for index matching. These steps were needed in the needle case because the sensing region was located directly at the fiber's cut end, unlike the catheter where a buffer of unused fiber reduced end reflections. The sensor-embedded nitinol tube was then inserted and secured to a 20 cm long 18G (1.3 mm OD) nitinol MRI-compatible needle (KIM18/20, Innovative Tomography Products GmbH, Germany). The sensorized catheter setup is shown in Fig. 1b, and the final needle assembly in Fig. 1c.

B. Shape sensing theory

Distributed strain measurements followed established OFDR procedures [7], [22], balancing spatial resolution and sensitivity through the sliding window size: larger windows improve sensitivity by using more data but reduce spatial resolution by lengthening the sensor segment [25], [26]. This work investigates the impact of spatial resolution on calibration and validation outcomes, with experiments conducted asynchronously and processed in MATLAB.

For the sensorized catheter, distributed wavelength data from each fiber was measured separately with an Optical Vector Analyzer (OVA 5000, Luna) in both reference and sampling states. Local strain ε applied to each fiber was then calculated from the Bragg wavelength λ , the wavelength shift $\Delta\lambda$, and the effective photoelastic coefficient p_e (see Eq.(1)):

$$\varepsilon = \frac{\Delta\lambda}{\lambda(1 - p_e)}. \quad (1)$$

For the sensorized needle, raw time-domain signals were acquired individually for each fiber in both reference and sampling states using Luna Innovations' Optical Distributed Sensor Interrogator (ODiSI-B). OFDR processing in MATLAB then yielded distributed strain measurements for all fibers. Spectral resolution was artificially improved through spatial domain zero padding interpolation [27], and precision of cross-correlation peak determination was increased using a quadratic fit. Strain signals were smoothed using a moving window.

From Eq.(2), spectral shifts obtained by OFDR are proportional to temperature (T) and strain variations, with proportionality constants K_T and K_ε [28]. Due to the proximity of the fibers, it was assumed, and shown in [22], that all three fibers experienced the same local temperature variations and axial stresses. These effects were accounted for in the strain offset ε_0 (see Eq.(3)).

$$\Delta\lambda = K_T\Delta T + K_\varepsilon\Delta\varepsilon. \quad (2)$$

A geometric model (Fig. 1a) based on trigonometric equations, inspired by Froggatt et al. [29], calculates the sensor's 3D spatial coordinates. Sensor segments are defined by spatial resolution Δx , curvature κ , and orientation α . Local strain for each fiber is also determined by its distance from the neutral axis (r) and transverse angular position (ϕ) (see Eq.(3)). The sensor's transversal geometric parameters

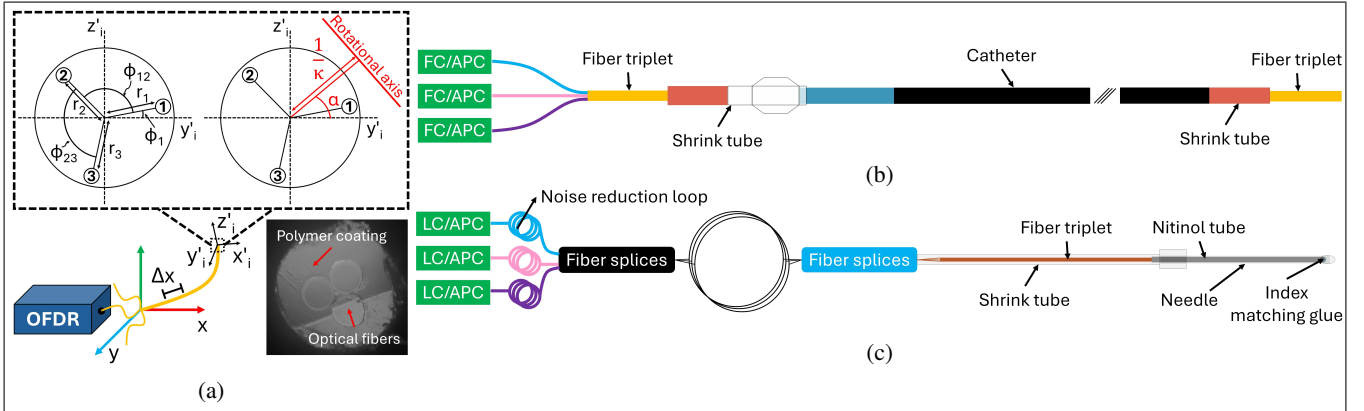


Fig. 1: (a) Geometric model for shape recovery in the tracking frame (x, y, z) defines sensor segments by spatial resolution Δx , with each segment described by curvature κ , orientation α , and local coordinates (x'_i, y'_i, z'_i) . The three sensor fibers are characterized by their distance from the neutral axis (r) and transverse angular position (ϕ). A microscopic image shows the sensor's cross-section [22]. (b) Sensorized catheter and (c) needle assemblies.

are replaced with their values, which must first be mapped across the detection length using a calibration approach:

$$\begin{aligned}\epsilon_1 &= -\kappa r_1 \sin(\alpha + \phi_1) + \epsilon_0 \\ \epsilon_2 &= -\kappa r_2 \sin(\alpha + \phi_1 + \phi_{12}) + \epsilon_0 \\ \epsilon_3 &= -\kappa r_3 \sin(\alpha + \phi_1 + \phi_{12} + \phi_{23}) + \epsilon_0.\end{aligned}\quad (3)$$

Curvature and orientation of each sensor segment are determined by solving a nonlinear system, formed by subtracting pairs of strain measurements from the three fibers (i.e. $\epsilon_{ij} = \epsilon_i - \epsilon_j$; $i, j = 1, 2, 3$), which cancels the bias ϵ_0 , thereby eliminating temperature and axial strain effects. The slope of each segment is determined by a linear relationship between curvature and segment length, expressed as $\Delta\theta_i = \kappa_i \Delta x = \frac{\Delta x}{\rho_i}$. The end position of segment i in its local coordinate system is then calculated using its slope and curvature radius ρ_i with Eq.(4):

$$P_i^j = [\rho_i \sin(\Delta\theta_i), 0, -(\rho_i - \rho_i \cos(\Delta\theta_i))]^T. \quad (4)$$

The end positions of all segments in global coordinates are derived by projecting the local coordinates of each segment. This is achieved through successive rotations by angle α , incrementally reconstructing the sensor's 3D shape [7], [11].

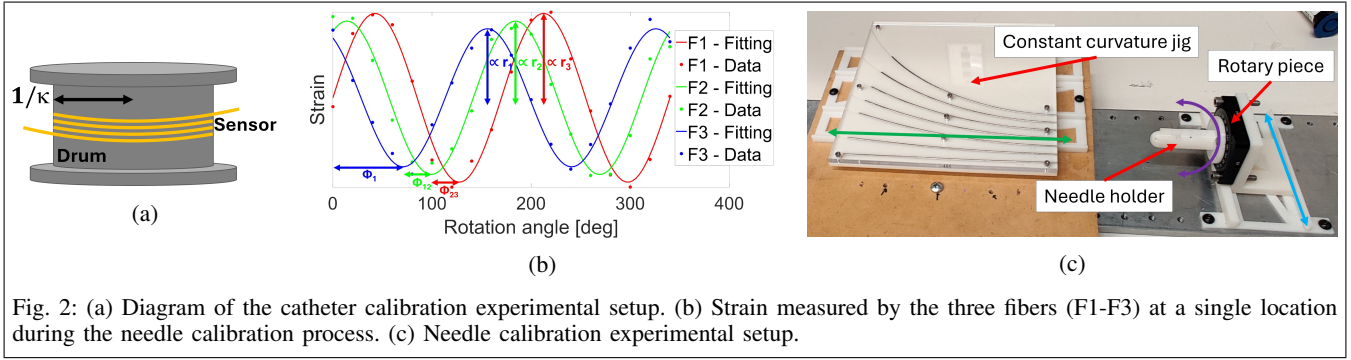
C. Catheter calibration

Catheters, designed to navigate inside blood vessels or body cavities without causing damage, come in various sizes and are made of flexible, biocompatible materials. Sensing points in all three fibers, corresponding to the segments defined by the chosen spatial resolution, were registered using strain peaks induced by the heat from the tip of a soldering iron for references. The calibration derived the sensor's ϕ_1 angle and adjusted the deformation constant K_e by reversing shape recovery steps. Given the catheter's length and flexibility, assumptions were made regarding the transversal positions of the fibers along the sensor. The extrusion process helped maintain the fibers in a stable position, ensuring relatively consistent distances from the sensor's neutral axis

and angles, as shown in the Supplementary Material of [22]. The distances to the neutral axis, $r_{1,2,3}$, and the relative angles, ϕ_{12} and ϕ_{23} , were assumed to be constant along the catheter and were set to $70\mu\text{m}$ and 120° , respectively, based on the sensor's cross-section. Only ϕ_1 , representing a global rotation of the fiber triplet caused by extrusion, was estimated through calibration. Strain signals from the fibers were measured after the catheter was tightly coiled around three drums (Fig. 2a), each with curvatures of 9.52, 12.22, and 25.34 m^{-1} , respectively. The catheter was wrapped seven separate times on each drum, with careful attention to minimize any twisting during the process. The acquisitions were divided into two sets: one for calibration and one for validation. All acquisitions from the two larger drums were used exclusively for validation, while two acquisitions from the smallest drum were reserved for calibration. The smaller drum's larger curvature allowed for clearer bending strain measurements, making it easier to identify the calibration parameters. The same procedure for determining curvature and orientation with the model's equations was applied, but with ϕ_1 estimated and the deformation constant refined to account for possible discrepancies in the presumed neutral axis distance to each fiber, using known reference values for orientation and curvature. Results were averaged across the two calibration acquisitions and smoothed using a moving window. Using the calibrated values of ϕ_1 and K_e , shapes from the validation dataset were reconstructed at five spatial resolutions (1 mm to 1 cm). The resulting 3D coordinates were compared to expected values following point-cloud registration using the RMSE metric.

D. Needle calibration

Surgical needles, made of rigid stainless steel or metal alloys for a sharp, durable tip, are designed to penetrate tissue with minimal resistance. They vary in length and gauge sizes, with 20 cm being standard for prostate interventions. Sensing points were registered by detecting natural backscatter signal drops at the fiber ends near the needle tip, which served



as reference points. Compared to the catheter, the needle's shorter length and rigidity allowed for additional calibration steps for greater precision.

Inspired by Roesthuis et al. [30], all the needle's geometric parameters were characterized at each sensor segment. The needle is bent to a set curvature and rotated about its central axis, causing sinusoidal strain variations in each fiber. The curve-fitted resulting strain curves are analyzed to derive the fibers' local geometric parameters by examining the amplitude and phase of their sinusoidal deformation. An example of sinusoidal strain patterns is shown in Fig. 2b. This process is repeated for all sensing locations.

The sensorized needle was deflected using 3D-printed (Stratasys F170 printer) ABS jigs with 13 grooves of constant curvatures (0 to 4 m^{-1}), filled with 16G (1.7 mm OD) hollow needles. The needle was inserted into each groove 18 times, at angles from 0° to 350° in 20° increments. A custom 3D-printed XY linear setup, seen in Fig. 2c, allowed for easier needle movement and precise rotation. The needle's bending curvatures were divided into two sets: one for calibration (0.25, 0.5, 1, 1.6, 2, 2.5, 3.2, and 4 m^{-1}) and one for validation (0.8, 1.25, and 3.125 m^{-1}).

According to beam theory [31], the boundary conditions at the needle tip cause no deformation, explaining the gradual decrease in deformation towards the sensor tip even when bent at a constant curvature during calibration. To accurately recover the sensor's geometrical parameters and perform shape sensing, an ad-hoc deformation signal analysis was developed to correct for nonlinear curvature near the needle tip. Similar to the catheter approach, the uniform fiber arrangement along the sensor allowed for assuming constant distances to the neutral axis and relative angles, which, combined with known needle orientation, solved the model's equations to recover needle curvature. Longitudinal output-to-ground-truth curvature ratios were averaged across all same groove acquisitions.

Using calibrated geometrical parameters and the corrective approach for nonlinear tip curvature, shapes from the validation dataset were reconstructed at five spatial resolutions (1 mm to 1 cm) to assess their impact on shape recovery. Distal curvature discrepancies due to boundary conditions were corrected by extrapolating adjustments from proximal curvature, quantified during calibration. The resulting 3D coordinates were compared to expected values using the

RMSE metric.

III. RESULTS AND DISCUSSION

A. Catheter calibration

The calibrated values of ϕ_1 and K_e over 40.6 cm (centered along the 1 m catheter) are plotted in Fig. 3a. With K_e averaging near 1, the chosen geometrical parameters appear to be accurate approximations of the actual values. Fig. 5a shows the 3D shape reconstruction errors for the validation dataset, with average RMSEs of $0.91 \pm 0.44 \text{ mm}$, $2.41 \pm 0.39 \text{ mm}$, and $1.69 \pm 0.45 \text{ mm}$ at curvatures of 9.52, 12.22, and 25.34 m^{-1} , respectively. The overall average RMSE is $1.67 \pm 0.77 \text{ mm}$ ($0.4\% \pm 0.2\%$) across all curvatures and spatial resolutions.

Fig. 5a shows that the impact of spatial resolution is relatively limited across curvatures of 9.52 and 12.22 m^{-1} . For 25.34 m^{-1} curvature, a 1 mm resolution yields better results than 5 mm, 8 mm, or 10 mm, likely because the latter resolutions don't improve sensitivity enough to offset the loss in spatial resolution. Since larger curvatures are inherently easier to detect, a smaller resolution proves more effective in this scenario. Among the larger resolutions, however, 10 mm seems to provide a better balance than 8 mm. A 3 mm spatial resolution consistently yields the best results across all curvatures, indicating it offers the optimal balance between resolution and sensitivity.

The smallest errors were observed at a curvature of 9.52 m^{-1} , while the largest occurred at 12.22 m^{-1} . Although larger curvatures improve the SNR, one main factor contributing to reconstruction inaccuracy is the iterative, segment-by-segment shape reconstruction process from the sensor base. Errors in each segment propagate to the next, accumulating along the reconstruction path. This effect is amplified by larger local error, which increases with curvature, as shown in [22]. This would explain why errors at 12.22 m^{-1} are greater than those at both 9.52 m^{-1} (less accumulated error) and 25.34 m^{-1} (enhanced SNR). Additionally, the errors at 9.52 m^{-1} may be lower than those at 25.34 m^{-1} because reduced error accumulation compensates for the lower SNR. Experimental factors such as variability in manual catheter placement, external torsion, and residual internal fiber twist may have contributed to outliers in the results.

Using the performed calibration failed to accurately recover the shape of the catheter overlaid on a 2D sine curve printed on millimetric paper, more specifically the second half of the wave. To investigate this discrepancy, the calibration was repeated with the sine wave as a reference, and the ϕ_1 results were compared to those obtained using drums for a round reference shape.

The average ϕ_1 results from the sine curve, obtained across four acquisitions, differ significantly from the drum results in regions where the curvature passes through zero, as shown in Fig. 3b. The discrepancy in the central region of the curve, where the curvature transitions through zero to change direction, significantly impacts subsequent values in the sine curve's second hump, despite following the same trend as the drum results. Likely causes include inadequacies in the shape reconstruction model for describing null curvature regions, or increased sensor torsion and signal loss from the more complex shape. These findings highlight the need for torsion compensation and suggest that calibrating with complex shapes, like 3D shapes, with varying curvature could improve accuracy by addressing factors that simpler calibration shapes overlook, especially for reconstructing shapes with multiple inflection points like sinusoidal curves.

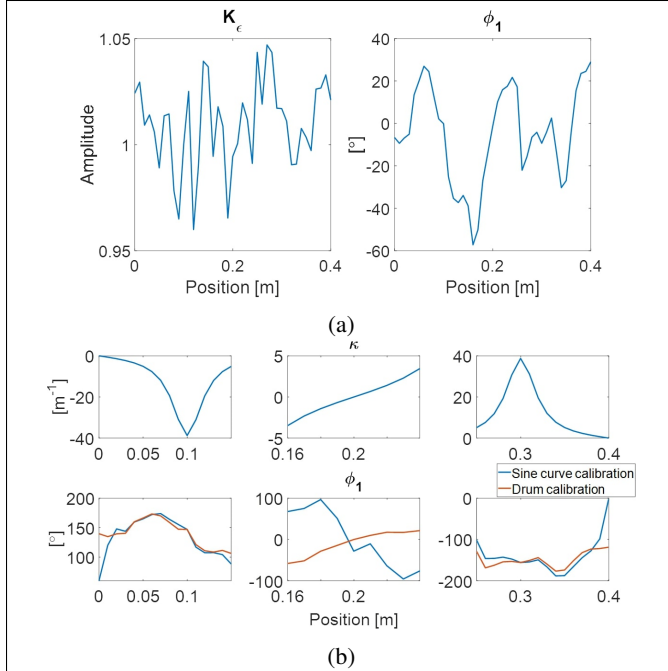


Fig. 3: (a) Calibration parameters results for the catheter. (b) Theoretical curvature of the sine curve (first row) and ϕ_1 results from drum calibration overlaid and aligned to those from sine curve calibration (second row). The results are presented at a spatial resolution of 10 mm.

B. Needle calibration

During calibration and validation, only 120 mm of the 200 mm sensorized needle was used. This choice was based on two factors: prior experiments reconstructed only the 120 mm inserted into tissue [32], and beam theory requires correction for nonlinear curvature due to boundary conditions near the needle's base in addition to the tip, which was

outside the scope of this study.

To establish the required adjustments, the experimental nonlinear behavior of needle tip curvature was quantified. Initially, output-to-real curvature ratios were fitted to third-degree polynomials for curvatures from 0.25 to 1.6 m^{-1} and exponential base 2 functions for curvatures from 1.6 to 4 m^{-1} , optimizing the coefficients of determination. Fig. 4a shows the fitted curvature ratios. Subsequently, curvature-dependent trends in the ratio coefficients (p_1 - p_4 and a - d) were further analyzed using third-degree polynomial curve fitting, as seen in Fig. 4b-4c. Using the new corrective approach, strain signal amplitudes near the needle tip were adjusted, and sensor geometric parameters for each segment were calculated as outlined in Section II-D. The results were then smoothed using a moving window and averaged across the calibration dataset, culminating in the results plotted in Fig. 4d.

The 3D shapes of the validation dataset were reconstructed using the calibrated geometric parameters and the curvature correction strategy, with errors shown in Fig. 5b. Average RMSE values were 0.14 ± 0.06 mm, 0.21 ± 0.11 mm, and 0.35 ± 0.14 mm at curvatures of 0.8, 1.25, and 3.125 m^{-1} , respectively. An overall average RMSE of 0.23 ± 0.14 mm ($0.2\% \pm 0.1\%$) was achieved across all curvatures and spatial resolutions.

As with the catheter, Fig. 5b suggests that spatial resolution has minimal impact. At curvatures of 0.8 and 1.25 m^{-1} , a finer resolution corresponds to lower RMSE. At 3.125 m^{-1} , resolutions of 3 mm and 5 mm show larger RMSE compared to 8 mm and 10 mm, likely due to insufficient sensitivity improvement. Across all curvatures, a 1 mm resolution consistently delivers the best results. Variation in RMSE across spatial resolutions may be influenced by the tip nonlinear curvature correction strategy. Curve fittings during its development yielded varying coefficients of determination depending on spatial resolution, likely affecting reconstruction accuracy. Fig. 5b shows smaller curvature correlates with lower RMSE. As previously mentioned, shapes with higher curvature can lead to greater errors. For surgical needles, curvatures $< 1.5 m^{-1}$ hold greater significance in clinical applications.

C. Catheter-Needle Comparison

Tool calibration must consider the distinct characteristics of the catheter and surgical needle. The catheter, being longer, more flexible, and sensitive to torsion, required a simplified calibration, which made the process faster. However, these features as well as larger bending and lack of torsion compensation led to higher RMSEs, likely requiring recalibration before each use. In contrast, needle calibration involves multiple bending amplitudes and orientations, but benefits from better sensor embedding stability and thus repeatability, allowing for reuse across experiments. In clinical scenarios where the central region of the catheter is key, calibration can ignore boundary conditions, unlike the needle, which require corrective methods that can introduce errors. Yet, when full-shape accuracy is needed, a more refined,

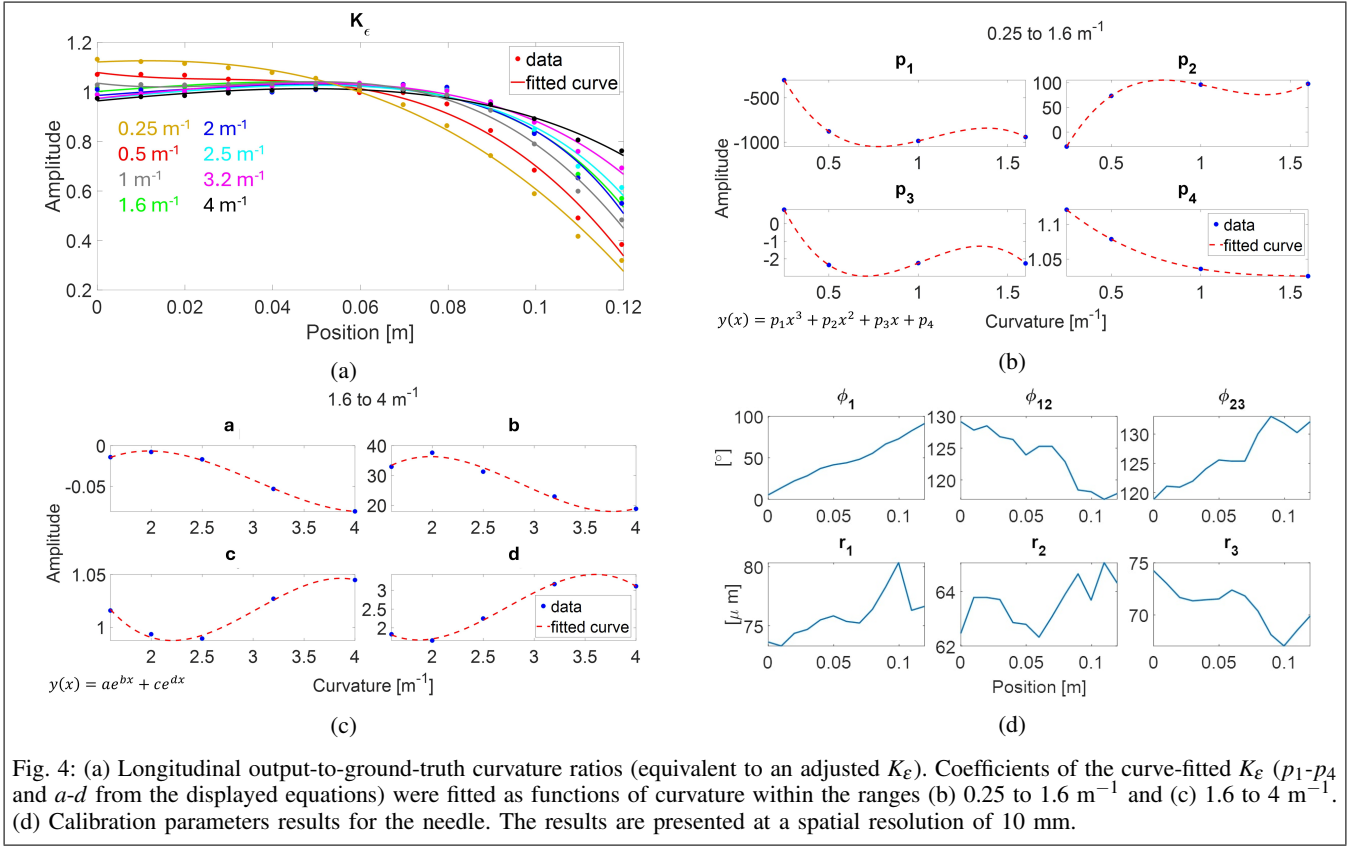


Fig. 4: (a) Longitudinal output-to-ground-truth curvature ratios (equivalent to an adjusted K_ϵ). Coefficients of the curve-fitted K_ϵ (p_1 - p_4 and a - d from the displayed equations) were fitted as functions of curvature within the ranges (b) 0.25 to 1.6 m^{-1} and (c) 1.6 to 4 m^{-1} . (d) Calibration parameters results for the needle. The results are presented at a spatial resolution of 10 mm.

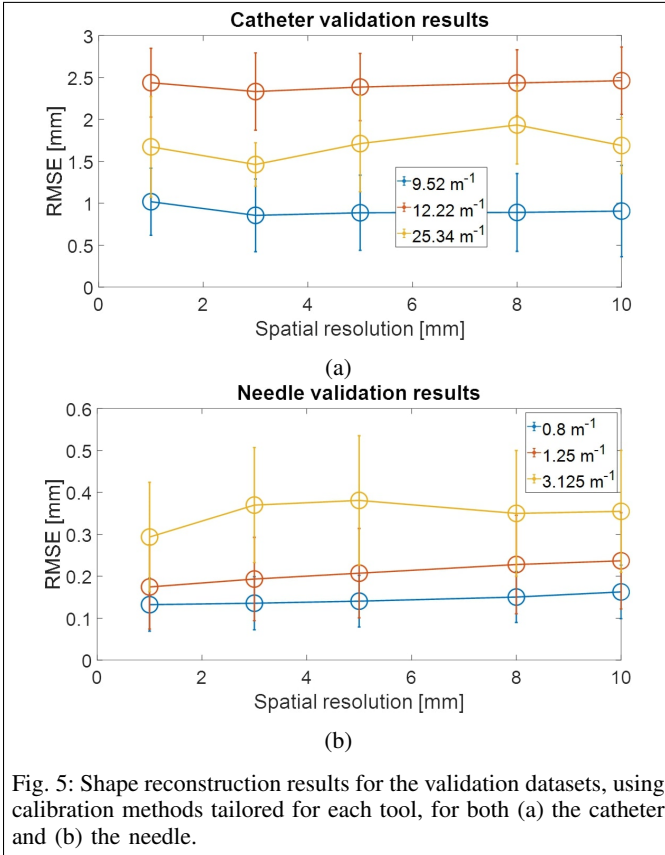


Fig. 5: Shape reconstruction results for the validation datasets, using calibration methods tailored for each tool, for both (a) the catheter and (b) the needle.

needle-like calibration would be beneficial, despite the added complexity and time. Catheters must handle more complex shapes and multiple inflection points, demanding torsion compensation and refined calibration strategies. While less crucial for needles, improving reconstruction accuracy for shapes with multiple inflection points could expand their clinical versatility. Lastly, although spatial resolution does not significantly affect accuracy, its optimal value still depends on the tool and medical application. Overall, needle calibration is more robust, but catheter calibration is faster and simpler in practice.

IV. CONCLUSION

This work presents two calibration techniques for precise 3D shape reconstruction tailored to a catheter for intravascular procedures and a flexible surgical needle for prostate interventions. The calibration processes are thoroughly detailed, addressing the specific needs of each instrument. Catheter calibration demonstrated clinically acceptable error margins across various curvatures and resolutions, although complex shapes, such as sinusoidal curves, highlight the need for advanced models to address torsion and null curvature regions. Needle calibration, enhanced by curvature correction near tool boundaries, demonstrated greater precision. While the introduced techniques provide a strong foundation, further refinement is required to better handle large curvature, multiple inflection points, and torsional effects in clinical settings.

ACKNOWLEDGMENT

The authors thank Anthony Roberge and Boston Scientific Corporation for their contributions in fabricating the sensor, and Frédéric Monet and Dimitri Lezcano for their valuable insights and guidance. The authors declare no conflicts of interest related to this research.

REFERENCES

- [1] The Johns Hopkins University, The Johns Hopkins Hospital, and Johns Hopkins Health System, "Percutaneous transluminal angioplasty," 2021. [Online]. Available: <https://www.hopkinsmedicine.org/health/treatment-tests-and-therapies/percutaneous-transluminal-angioplasty>
- [2] I. Floris, J. M. Adam, P. A. Calderón, and S. Sales, "Fiber optic shape sensors: A comprehensive review," *Optics and Lasers in Engineering*, vol. 139, p. 106508, 2021. [Online]. Available: <https://www.sciencedirect.com/science/article/pii/S0143816620319461>
- [3] S. Banerjee, K. Sarode, A. Patel, A. Mohammad, R. Parikh, E. J. Armstrong, S. Tsai, N. W. Shammass, and E. S. Brilakis, "Comparative assessment of guidewire and microcatheter vs a crossing device-based strategy to traverse infrainguinal peripheral artery chronic total occlusions," *J Endovasc Ther*, vol. 22, no. 4, pp. 525–34, 2015.
- [4] T. Penzkofer, K. Tuncali, A. Fedorov, S. E. Song, J. Tokuda, F. M. Fennessy, M. G. Vangel, A. S. Kibel, R. V. Mulkern, W. M. Wells, N. Hata, and C. M. Tempany, "Transperineal in-bore 3-t mr imaging-guided prostate biopsy: a prospective clinical observational study," *Radiology*, vol. 274, no. 1, pp. 170–80, 2015.
- [5] N. Stone and E. D. Crawford, *The Prostate Cancer Dilemma: Selecting Patients for Active Surveillance, Focal Ablation and Definitive Therapy*. Springer, 2016.
- [6] B. Lee, "Review of the present status of optical fiber sensors," *Optical fiber technology*, vol. 9, no. 2, pp. 57–79, 2003.
- [7] M. Froggatt and J. Moore, "High-spatial-resolution distributed strain measurement in optical fiber with rayleigh scatter," *Applied Optics*, vol. 37, no. 10, pp. 1735–1740, 1998. [Online]. Available: <http://opg.optica.org/ao/abstract.cfm?URI=ao-37-10-1735>
- [8] F. Parent, S. Loranger, K. K. Mandal, V. L. Iezzi, J. Lapointe, J.-S. Boisvert, M. D. Baiad, S. Kadoury, and R. Kashyap, "Enhancement of accuracy in shape sensing of surgical needles using optical frequency domain reflectometry in optical fibers," *Biomedical Optics Express*, vol. 8, no. 4, pp. 2210–2221, 2017. [Online]. Available: <https://opg.optica.org/boe/abstract.cfm?URI=boe-8-4-2210>
- [9] K. K. Mandal, F. Parent, S. Martel, R. Kashyap, and S. Kadoury, *Calibration of a needle tracking device with fiber Bragg grating sensors*, ser. SPIE Medical Imaging. SPIE, 2015, vol. 9415. [Online]. Available: <https://doi.org/10.1117/12.2081198>
- [10] K. Song, D. A. Lezcano, G. Sun, J. S. Kim, and I. I. Iordachita, "Towards automatic robotic calibration system for flexible needles with fbg sensors," in *2021 International Symposium on Medical Robotics (ISMR)*, 2021, Conference Proceedings, pp. 1–7.
- [11] R. J. Roesthuis, M. Kemp, J. J. v. d. Dobbelsteen, and S. Misra, "Three-dimensional needle shape reconstruction using an array of fiber bragg grating sensors," *IEEE/ASME Transactions on Mechatronics*, vol. 19, no. 4, pp. 1115–1126, 2014.
- [12] D. A. Lezcano, Y. Zhetpissov, A. Cheng, J. S. Kim, and I. I. Iordachita, "Optical fiber-based needle shape sensing in real tissue: Single core vs. multicore approaches," *arXiv preprint arXiv:2309.04407*, 2023.
- [13] C. Li, L. Zhang, X. Zhang, G. Liu, and J. Zhao, "A compliant actuator for steering the needle within tissue with feedback of fbg-based shape sensing," *Sensors and Actuators A: Physical*, vol. 356, p. 114340, 2023. [Online]. Available: <https://www.sciencedirect.com/science/article/pii/S0924424723001899>
- [14] L. Zhang, C. Li, H. Dong, X. Liu, T. Sun, K. T. Grattan, and J. Zhao, "Fiber bragg grating-based sensor system for sensing the shape of flexible needles," *Measurement*, vol. 206, p. 112251, 2023.
- [15] K. Mandal, F. Parent, S. Martel, R. Kashyap, and S. Kadoury, "Vessel-based registration of an optical shape sensing catheter for mr navigation," *International Journal of Computer Assisted Radiology and Surgery*, vol. 11, no. 6, pp. 1025–1034, 2016. [Online]. Available: <https://doi.org/10.1007/s11548-016-1366-7>
- [16] F. Monet, S. Sefati, P. Lorre, A. Poiffaut, S. Kadoury, M. Armand, I. Iordachita, and R. Kashyap, "High-resolution optical fiber shape sensing of continuum robots: A comparative study," in *2020 IEEE International Conference on Robotics and Automation (ICRA)*, 2020, Conference Proceedings, pp. 8877–8883.
- [17] F. Parent, M. Gérard, F. Monet, S. Loranger, G. Soulez, R. Kashyap, and S. Kadoury, "Intra-arterial image guidance with optical frequency domain reflectometry shape sensing," *IEEE Transactions on Medical Imaging*, vol. 38, no. 2, pp. 482–492, 2019.
- [18] M. Megens, M. D. Leistikow, A. van Dusschoten, M. B. van der Mark, J. J. L. Horikx, E. G. van Putten, and G. W. t. Hooft, "Shape accuracy of fiber optic sensing for medical devices characterized in bench experiments," *Medical Physics*, vol. 48, no. 7, pp. 3936–3947, 2021. [Online]. Available: <https://aapm.onlinelibrary.wiley.com/doi/abs/10.1002/mp.14881>
- [19] S. M. Roodsari, S. Freund, A. Zam, G. Rauter, and P. C. Cattin, "Fabrication and characterization of a flexible fbg-based shape sensor using single-mode fibers," *IEEE Transactions on Biomedical Engineering*, vol. 69, no. 8, pp. 2488–2498, 2022.
- [20] F. Han, Y. He, H. Zhu, and K. Zhou, "A novel catheter shape-sensing method based on deep learning with a multi-core optical fiber," *Sensors*, vol. 23, no. 16, p. 7243, 2023. [Online]. Available: <https://www.mdpi.com/1424-8220/23/16/7243>
- [21] P. Lorre, F. Monet, M. Gauthier, A. Poiffaut, A. Roberge, S. Kadoury, and R. Kashyap, *Extruded complex optical fiber structures for shape sensing and biomedical applications (Conference Presentation)*, ser. SPIE OPTO. SPIE, 2020, vol. 11283. [Online]. Available: <https://doi.org/10.1117/12.2546814>
- [22] J. Francoeur, A. Roberge, P. Lorre, F. Monet, C. Wright, S. Kadoury, and R. Kashyap, "Optical frequency domain reflectometry shape sensing using an extruded optical fiber triplet for intra-arterial guidance," *Optics Express*, vol. 31, no. 1, pp. 396–410, 2023.
- [23] A. Roberge, S. Loranger, J.-S. Boisvert, F. Monet, and R. Kashyap, "Femtosecond laser direct-writing of high quality first-order bragg gratings with arbitrary complex apodization by phase modulation," *Optics Express*, vol. 30, no. 17, pp. 30405–30419, 2022. [Online]. Available: <http://opg.optica.org/oe/abstract.cfm?URI=oe-30-17-30405>
- [24] P. Lorre, F. Monet, M. Gauthier, A. Poiffaut, A. Roberge, S. Kadoury, and R. Kashyap, *Extruded optical fiber triplets for 3D shape sensing for minimally invasive surgery*, ser. Seventh European Workshop on Optical Fibre Sensors. SPIE, 2019, vol. 11199. [Online]. Available: <https://doi.org/10.1117/12.2541323>
- [25] C. Liang, Q. Bai, M. Yan, Y. Wang, H. Zhang, and B. Jin, "A comprehensive study of optical frequency domain reflectometry," *IEEE Access*, vol. 9, pp. 41 647–41 668, 2021.
- [26] S. Zhao, J. Cui, L. Suo, Z. Wu, D.-P. Zhou, and J. Tan, "Performance investigation of ofdr sensing system with a wide strain measurement range," *Journal of Lightwave Technology*, vol. 37, no. 15, pp. 3721–3727, 2019. [Online]. Available: <https://opg.optica.org/jlt/abstract.cfm?URI=jlt-37-15-3721>
- [27] F. Monet, S. Loranger, V. Lambin-Iezzi, A. Drouin, S. Kadoury, and R. Kashyap, "The rogue: a novel, noise-generated random grating," *Optics Express*, vol. 27, no. 10, pp. 13 895–13 909, 2019. [Online]. Available: <http://opg.optica.org/oe/abstract.cfm?URI=oe-27-10-13895>
- [28] Sensuron, "Fiber optic sensing fundamentals." [Online]. Available: <https://www.sensuron.com/fiber-optics-sensing-fundamentals/>
- [29] M. E. Froggatt and R. G. Duncan, "Fiber optic position and/or shape sensing based on rayleigh scatter," 4 September 2008. [Online]. Available: <https://patents.google.com/patent/US7772541B2/en>
- [30] R. J. Roesthuis, M. Kemp, J. J. van den Dobbelsteen, and S. Misra, "Three-dimensional needle shape reconstruction using an array of fiber bragg grating sensors," *IEEE/ASME transactions on mechatronics*, vol. 19, no. 4, pp. 1115–1126, 2013.
- [31] D. M. Parks and L. Anand, "Euler-bernoulli beams: Bending, buckling, and vibration," February 9 2004. [Online]. Available: <https://ocw.mit.edu/courses/2-002-mechanics-and-materials-ii-spring-2004/bc25a56b5a91ad29ca5c7419616686f7 lec2.pdf>
- [32] J. Francoeur, D. Lezcano, Y. Zhetpissov, R. Kashyap, I. Iordachita, and S. Kadoury, "Fully distributed shape sensing of a flexible surgical needle using optical frequency domain reflectometry for prostate interventions," in *2024 IEEE International Conference on Robotics and Automation (ICRA)*, 2024, pp. 17 594–17 601.